Thin Solid Films 692 (2019) 137536

Contents lists available at ScienceDirect

Thin Solid Films

journal homepage: www.elsevier.com/locate/tsf

Profiling As plasma doped Si/SiO_2 with molecular ions

H. Trombini[*,a], I. Alencar[1,a], G.G. Marmitt[2,a], R. Fadanelli[a], P.L. Grande[a], M. Vos[b], J.G. England[c,d]

[a] Instituto de Física, Universidade Federal do Rio Grande do Sul, Av. Bento Gonçalves 9500, Porto Alegre–RS CP 15051, Brazil
[b] Electronic Materials Engineering, Research School of Physics and Engineering, Australian National University, Australia
[c] Varian Semiconductor Equipment, Silicon Systems Group, Applied Materials Inc., 35 Dory Road, Gloucester, MA 01930, USA
[d] Surrey Ion Beam Centre, Advanced Technology Institute, University of Surrey, Guildford, Surrey GU2 7XH, UK

ARTICLE INFO

Keywords:
Plasma doping
Medium energy ion scattering
Molecular ions
Coulomb explosion
Depth profiling

ABSTRACT

Arsenic profiles in plasma doped silicon wafers were traced by scattering of H^+ and H_2^+ ions at medium energies. Two wafers were doped with the same bias, gas pressure, total implanted dose and AsH_3 concentration. After implantation, the wafers were submitted to industrial cleaning processes, resulting in the formation of a surface SiO_2 layer, and one wafer was subjected to an additional thermal treatment. Scattering spectra of single and molecular ion beams with the same energy per nucleon and charge state differed only by the energy broadening due to the break-up of the molecule, allowing depth profiling by calculation of the dwell time before the backscattering collision. For the SiO_2 layers of these samples a density reduction of, on average, 13% was observed, compared to thermally grown SiO_2. In addition, the arsenic depth-profile determined were in close agreement with independent findings obtained by electron techniques.

1. Introduction

Advances in complementary metal oxide semiconductor (CMOS) transistor technology have demanded new processes to fabricate novel devices and new methods to characterize the manufactured devices. In the last few years the architecture of leading-edge Field effect transistor (FET) has transitioned from conventional planar to 3D Fin (finFETs) [1]. This new architecture may include minimum dimensions smaller than 5 nm, creating new challenges for the characterization and metrology of increasingly sophisticated structures and materials [2,3]. One of these challenges concerns conformal doping of fin structures [4,5], where plasma doping (PLAD) has been proposed as a feasible dopant technique [6–8].

Among several characterization techniques, ion beam analysis is currently used to determine the dopant distribution [9,10] but is limited to provide the areal concentration in atoms per cm^2, *viz.* depth is indirectly obtained after a given value for the density of the layer is used. We have investigated the arsenic profile in plasma-doped silicon wafers using the scattering of H^+ and H_2^+ ions at medium energies, which allowed us to determine the thickness and density of the oxide overlayer separately. To demonstrate this method we used two wafers doped under the same conditions and the same industrial cleaning apart from an additional thermal treatment. The single and molecular ion beams had the same energy per nucleon, resulting in the same backscattering spectra *apart* from an energy broadening due to the break-up of the molecule. Under these conditions the depth profile can be extracted from the dwell time before the backscattering collision [11]. This procedure determine directly the absolute layer thickness and, hence, its density. SiO_2 layer growth after the cleaning step was observed for both samples and we showed here that the density of such layers was lower than for bulk, amorphous SiO_2. The arsenic depth profiles were in close agreement with independent results obtained from Transmission Electron Microscopy coupled with Energy-Dispersive X-ray Spectroscopy (TEM/EDS) and Electron Rutherford Backscattering Spectrometry (ERBS).

2. Materials and methods

2.1. PLAD process

Two sets of samples were produced with bare silicon wafers, biased at 7 kV. A full description of sample preparation is given elsewhere [12,13] and briefly summarized here. In short, these samples were implanted with arsenic in a VIISta PLAD system in Gloucester [14],

* Corresponding author.
E-mail address: henrique.trombini@ufrgs.br (H. Trombini).
[1] Present address: Departamento de Física, Universidade Federal de Santa Catarina, R. Eng. Agr. Andrei Cristian Ferreira s/n, Florianópolis–SC CEP 88040-900, Brazil.
[2] Present address: Afdeling Radiotherapie, Universitair Medisch Centrum Groningen, Fonteinstraat 18, Groningen 9713 GZ, Netherlands.

https://doi.org/10.1016/j.tsf.2019.137536
Received 18 June 2019; Received in revised form 9 August 2019; Accepted 4 September 2019
Available online 14 October 2019

using a plasma generated from a gas mixture containing AsH_3 to a total ion fluence of 1×10^{16} cm^2. In these two samples (S1 and S2), an SPM (sulphuric acid hydrogen peroxide mixture) wet chemical clean was performed which removed a large fraction of the As and formed an oxide layer on the Si. For S2, a "spike" anneal (1050 °C held for 1.7 s) was performed in a nitrogen atmosphere containing 100 ppm of oxygen.

2.2. Dopant profile metrology

Ion scattering experiments were carried out using the Medium Energy Ion Scattering (MEIS) facility at the Ion Implantation Laboratory (Universidade Federal do Rio Grande do Sul, Porto Alegre–RS, Brazil). A 500 kV electrostatic accelerator provided an incident beam of H^+ and H_2^+ with nominal energies of 200 keV per nucleon. The samples were mounted on a three-axis goniometer placed inside the analysis chamber, where a pressure of about 10^{-5} Pa is kept. Typical beam currents were smaller than 10 nA and 5 nA for the H^+ and H_2^+ ions, respectively, accumulating a total charge smaller than 90 μC/mm^2. The detection system consisted of a Toroidal Electrostatic Analyzer (TEA) collecting the backscattered H^+ ions. At the exit plane of the TEA a set of two micro-channel plates coupled to a position-sensitive detector allowed the determination of the scattering energy and angle for each impinging ion [15,16]. This detection system was centered at 120° with respect to the incident beam. The TEA angular aperture covered an angle of 24° and each angular bin corresponded to 0.08°. The overall energy resolution of the system was 450 eV for 100 keV H^+ ions.

Each measurement generated a two-dimensional heat-map (2D-map) of ion scattering yield as a function of energy and angle of the backscattered ions. 2D-map projection onto the energy axis was performed in order to facilitate the comparison to simulations and to access the goodness-of-fit using the χ^2_γ statistic [17]. For statistical improvement during the analysis, angular bins were summed up in an interval of a few degrees (4° and 2° for samples S1 and S2, respectively). Three different angular regions were selected: 108–112, 118–122 and 128–132° for S1 and 108–110, 117–119 and 126–128° for S2. While the angular regions selected for S1 are routinely chosen for data analyses, the regions selected for S2 avoid the loss of counts caused by the presence of blocking lines. Each resulting energy spectra was analyzed using the PowerMEIS code (available online) [18,19], which allowed for the standard profile quantifications in atoms/cm^2 of the As doping and the silicon dioxide (SiO_2) overlayers.

In addition, the absolute thicknesses and densities of the SiO_2 overlayers were determined from the break-up of H_2^+ ions following the procedure described previously [11,20]. By comparing the energy spectra from H^+ and H_2^+ at the same energy per nucleon, the H_2^+ broadening due to the Coulomb explosion was determined and converted to depth using the PowerMEIS code. The results obtained were compared to TEM/EDS and ERBS. Bright field TEM images and TEM/EDS profiles were made by commercial analytical laboratories on samples that had been coated with iridium before the TEM lamellae were produced [12]. Electron backscattering spectra were acquired with an electrostatic analyzer using highly mono-energetic beams produced from a barium oxide cathode and accelerated by a metal semi-sphere kept at high-voltage [21].

3. Results and discussion

Fig. 1 shows the 2D-map of ion scattering yield as a function of the backscattering angle and energy for samples S1 and S2 using 200 keV/u $H^+$and H_2^+ projectiles. The signals corresponding to arsenic (As) and silicon (Si), presented in the SiO_2 overlayer and the Si substrate, were well separated because of their large mass difference. Since the Si is at the surface its intensity depends strongly on the scattering angle according to the dependence of the kinematic factor. The leading edge of the As signal is much less sharp, indicating that it is located well below the surface. Below 175 keV, the Si signal increases again due to the contribution of the Si substrate. This signal drops dramatically at even lower energies (~ 170 keV) due to the channeling effect for the incident ions, which decreases the probability of the incident beam being backscattered. In addition, blocking lines are also visible in Fig. 1 (c and d) corresponding to a reduction of the ion scattering intensity for certain scattering angles (evident as vertical lines with reduced intensity). The presence of blocking lines in the As signal indicates that the As was substitutional into the silicon lattice after the thermal treatment performed on S2.

When comparing the spectra obtained for the same sample, the main difference between measurements with H^+ and H_2^+ ions concerns the width of the As signal. For H_2^+ ions, Coulomb explosion strongly affects the energy spectrum because of the mutual repulsion of the fragments after break-up of the molecule at the surface. Since it can simultaneously increase and decrease the speed of the fragments (as observed in the laboratory reference system) it causes extra energy broadening, called Coulomb-explosion broadening, which starts after the molecule break-up at the surface and ends at the backscattering collision, where one of the fragments is suddenly removed from its companion. The detected backscattered ions then have a broader energy-loss distribution [22], depending on the dwell time from the break-up event to the backscattering collision. This method allowed us to quantify the absolute thickness and therefore the density after using the standard MEIS analysis for H^+ [11]. Besides the Coulomb explosion, the stopping power of the fragments can also be affected by the correlated motion of the fragments after the break-up and before the backscattering collision. This is the so-called vicinage (or proximity) effect and arises from either an interference effect on the target excitation and ionization by the two projectiles or by the superposition of wake potentials [23]. Typically the vicinage effect for high energies increases the stopping power of a fragment by around 20% if the other fragment is nearby. This effect was also taken into account in the present analysis.

Initially, a standard MEIS analysis was performed for the experiments with H^+ ions, where the elemental distribution in S1 and S2 were quantified in atoms per cm^2. PowerMEIS simulations were performed with the differential-scattering cross section obtained by solving the orbit equation using the Ziegler–Biersack–Littmark interatomic potential [24], stopping powers from the SRIM library [25], and the energy straggling from the Chu model [26]. The neutralization fraction of the ions was obtained from the Marion and Young data [27] and an exponential modified Gaussian distribution was used to model the energy loss during the backscattering collision [28].

The thickness of the SiO_2 overlayer was then determined considering the additional broadening of the As signal measured with H_2^+ ions. In this case, PowerMEIS simulations were also carried out by keeping all parameters fixed from the H^+ simulations except the energy spread of the incoming beam since it was slightly worse from the Doppler effect from H_2^+ vibrations (450 eV for H^+ and 600 eV for H_2^+). It is important to consider these energy fluctuations associated with molecular vibrational levels in the incident molecular beam as it also contributes to the slope of the edge due to the energy resolution degradation. In addition, vicinage effect and Coulomb explosion broadening parameters had to be specified to allow PowerMEIS to simulate MEIS spectra for molecular projectiles. The vicinage effect parameter modified the stopping power along the incoming trajectory and was set to 1.24, an average value of the basically constant ratio in the energy per nucleon interval used in our experiments [29,30]. The Coulomb broadening used in the simulations as a function of depth for SiO_2 (Fig. 2) was calculated according to the procedure described in Ref. [20] using the Energy Loss Function (ELF) from Ref. [31]. The result is very similar to what would be expected for a Coulomb explosion without screening [11] and it was included in the PowerMEIS code using the parameters displayed in Fig. 2. The code convoluted the energy-loss distribution of the ions along the incoming trajectory using a

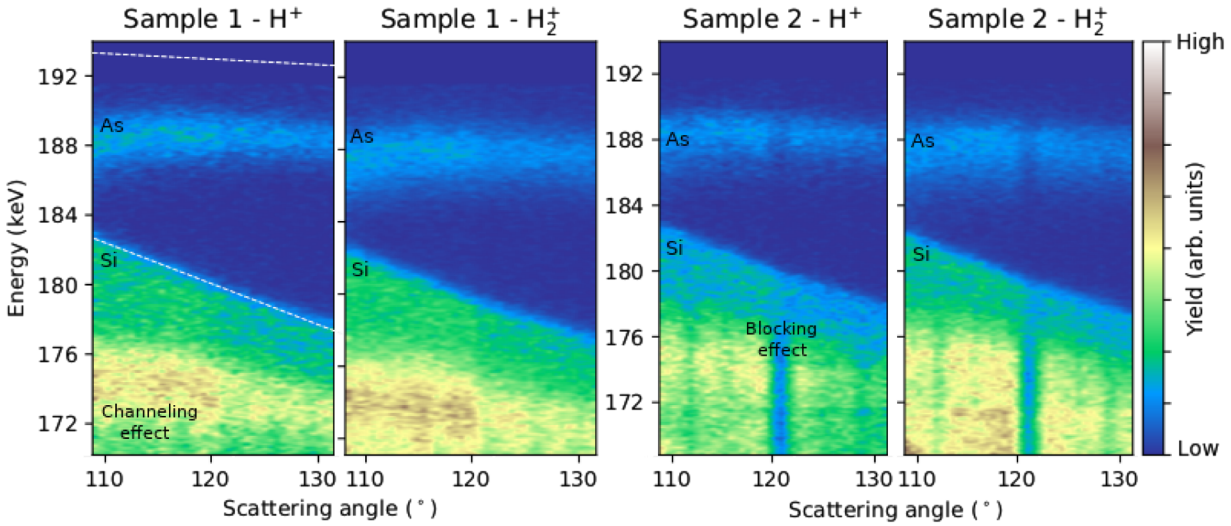

Fig. 1. MEIS 2D-map for samples S1 (a and b) and S2 (c and d) measured with 200 keV/u H^+ and H_2^+ ions. The signals from ions backscattering from As and Si are indicated as well as the yield reduction caused by channeling and blocking effects. The energy broadening of the As signal due to the Coulomb explosion is clearly visible. The oxygen signal was not measured and would start to appear at 165 keV.

step function, Eq. (2) from Ref. [20], and the standard deviation (broadening) from Fig. 2. A much simpler analysis could also be performed, where the Coulomb explosion broadening is taken directly from the subtraction of the variance of the As signals of the H^+ and H_2^+ ion beams after correction for the Doppler effect. From the Coulomb broadening, the SiO_2 thickness can be obtained directly from Fig. 2, as discussed in Ref. [11]. Both methods gave similar results but the PowerMEIS simulations were as accurate and reliable as the stopping power allows once they included all physical ingredients involved, *i.e.* the proper depth dependent Coulomb broadening and vicinage effects [20].

Fig. 3 shows the best models (a and e) used to describe S1 and S2, respectively. The models used to describe samples 1 and 2 were obtained through the analysis of three different backscattering angles. The

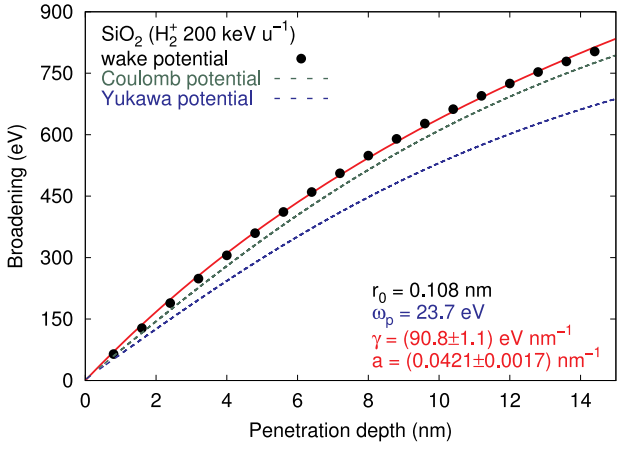

Fig. 2. Coulomb explosion broadening as a function of depth traversed by the molecular fragments of H_2^+ in ultra-thin SiO_2 films. The energy of the H_2^+ molecule was 200 keV/u. Dashed lines represent calculations of the Coulomb broadening assuming a pure Coulomb repulsive potential (green) and the Yukawa potential (blue). Filled circles represent calculations assuming a wake potential. Red line is a fit of wake potential data with the equation $\sigma_c = (\gamma x)/(1 + ax)$, where γ and a represent the Coulomb explosion linear and non-linear factor, respectively, and x the depth. These parameters were used for the MEIS simulation. r_0 is the interatomic separation in H_2^+ molecule and ω_p the plasmon energy. (For interpretation of the references to color in this figure legend, the reader is referred to the web version of this article.)

reduced Chi-square analysis was repeated for all three angular ranges. The projection of the 2D-map onto the energy axis for the angular aperture of 118–122° (b and c) and 117–119° (f and g) is presented for the H^+ (b and f) and H_2^+ (c and g) ion beams. The black open circles correspond to the experimental data and the blue line to the PowerMEIS simulations. From these results, it is possible to see good agreement between experimental and simulations down to 172 keV (S1) and 177 keV (S2), where channeling effects come into play and they are not described by the PowerMEIS simulations. The arsenic signal was clearly wider for H_2^+ than for H^+ in both samples. S2 shows a larger diffusion tail of As into Si compared to S1. Fig. 3 (d and h) present the chi-square analyses for H_2^+ ions performed for S1 and S2, respectively. This analysis was carried out by keeping constant the number of atoms per cm^2 obtained in the analysis with H^+ but varying the thickness (and consequently density) of the SiO_2 layer. It is pointed out that the combination of thickness and density by keeping their product constant only affects the H_2^+ spectra. The uncertainty associated with the broadening amounts to $\sim$ 50 eV, which corresponds to 1 nm according to Fig. 2 at 600 eV. Accordingly, a 9 $\pm$ 7 % increase in the thickness of the SiO_2 layer was obtained for S1 corresponding to a decrease in density compared to the nominal (bulk) SiO_2 density of 2.2 g/cm^3. For S2 this variation was even greater and corresponds to 17 $\pm$ 7%. Full descriptions of S1 and S2 samples after the analysis with H_2^+ are presented in Table 1. Such descriptions are in close agreement to previously published results employing He^+ ion beams [12,13,32]. The main difference is in the total amount of As, which is smaller here because of the much longer time elapsed between the sample preparation and measurements [13].

Fig. 4 (a and b) show the comparison between the results obtained by MEIS and TEM/EDS for S1 and S2. The red, black and blue lines correspond to the concentration (10^{22} atoms/cm^3) of oxygen, silicon and arsenic as obtained by MEIS, assuming stoichiometric SiO_2. The red, black and blue dots correspond to the atomic fraction of O, Si and As as obtained by TEM/EDS. The difference in heights is due to the different scales. The sample S1 that underwent only a wet clean process shows a SiO_2 layer of 11.0 nm with a reduced density of 2.00 g/cm^3 followed by a $As_{0.01}Si_{0.33}O_{0.65}$ layer of 2.75 nm with a similar density reduction. The outer Si layer, that contains the highest concentration of As, has been amorphized by the implantation. The sample S2 that underwent both wet clean and thermal treatment processes shows a SiO_2 layer of 12.4 nm with a reduced density of 1.83 g/cm^3 followed by a $As_{0.01}Si_{0.33}O_{0.65}$ layer of 1.2 nm with 1.86 g/cm^3 density. The layer

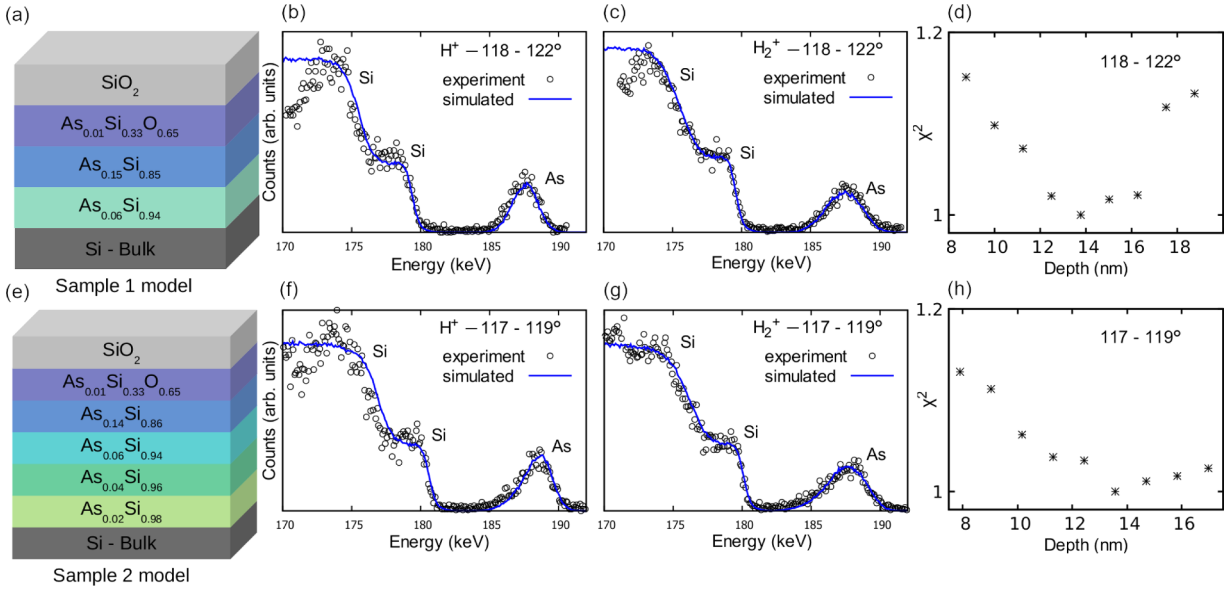

Fig. 3. MEIS results and analysis. Illustration of the best model obtained for S1 (a) and S2 (e). Projection of the 2D-map on the energy axis for the angular aperture of 118–122° (b and c) and 117–119° (f and g) for H^+ (b and f) and H_2^+ (c and g) ion beams. Reduced chi-square as a function of depth for S1 (d) and S2 (h).

with the highest concentration of As is now crystalline and some As has diffused to larger depths.

Concerning the implanted As, we estimated a total dose of $\sim 2.1 \times 10^{15}$ atoms/cm^2 for S1 and $\sim 2.7 \times 10^{15}$ atoms/cm^2 for S2, which is around one fourth of the nominal dose (1.0×10^{16} atoms/cm^2). Such discrepancies may be explained from the fact that during plasma doping processes a mass selector is not used and, therefore, a mix of compounds and neutral species are deposited on the substrate surface [8]. Thus, when placed close to a sample, the Faraday detector measured all the charged compounds [33]. Moreover, comparing the present results with previous MEIS measurements performed immediately after the sample preparation [12], we estimated a 20 % As loss in our samples. The larger amount of As observed in S2 is possibly related to the lower diffusivity of substitutional As in the silicon lattice. The TRIDYN code [34], which calculates the magnitudes of the ionic and neutral fluxes that occur during the PLAD implantation, predicts $\sim$ 12 nm under-dense SiO_2 layer for post-clean sample. This is in good agreement with our results. It also suggests that the oxide density decreases towards the surface as a consequence of ion beam mixing [12,32].

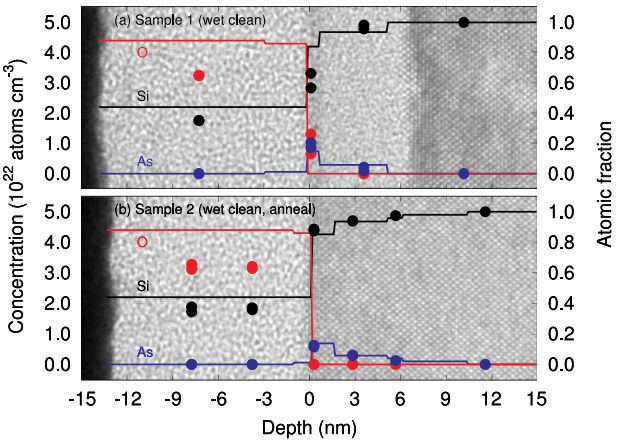

Fig. 4. Depth profiles obtained by MEIS (lines) quoted as atomic concentration and TEM/EDS (dots) quoted as atomic fraction for S1 (a) and S2 (b). At the background of each plot, TEM images of the samples are placed in scale.

The same samples were measured using 40 keV electrons scattered over 135°. The results are shown in Fig. 5. At low energy losses this technique resolves the mass of the scattering atoms (so called Electron Rutherford Backscattering or ERBS). At larger energy losses the energy is mainly determined by electronic excitation, and one does not resolve anymore the mass of the atom that scattered the projectile electron over 135°. As a reference we show the corresponding spectra of pure Si and pure SiO_2 in Fig. 5 (a). The recoil loss for scattering of 40 keV electrons over 135° from Si is 2.77 eV, from O 4.86 eV and As 1.04 eV. Note that the plasmon peak (for pure Si at $\sim$ 20 eV) is at an energy loss that corresponds to the sum of the recoil loss (2.77 eV) plus the plasmon excitation energy ($\sim$ 17 eV).

Only if the projectile-electron scatters from a nucleus towards the detector without the excitation of a plasmon on the way in or out does the electron contribute to the elastic peak. The thickness contributing to the elastic peak is thus of the order of the electron inelastic mean free path. The electronic excitations that cause the stopping in MEIS can be observed in the electron spectra directly, and indirectly at larger energy losses, but these excitations will also determine the height of the elastic peak of the different elements.

Spectra from S1 in Fig. 5 (b and c) show 3 peaks with the expected separation for As, Si and O. The O peak was less intense in S1 than for pure SiO_2 especially when the incoming beam impinged along the surface normal. Thus, the Si substrate also contributed to the spectrum. When the sample was rotated over 34°, then, the measurement was performed in a more surface-sensitive geometry and the height of the O peak increased relative to that of Si as the contribution of the Si substrate was smaller. The height of the As peak (relative to the O peak) decreased in the surface-sensitive geometry, indicating that the As was (on average) at larger depth than the O atoms. The electron scattering spectra from S2 were very similar to those of S1.

There was some variability in these measurements, presumably due to channeling (Kikuchi effect) that affects the backscattering intensity when the electrons interact with the single-crystal Si substrate. However, the same general trend was always observed. The spectra can be simulated as well with the PowerMEIS code [18,19], as most of the underlying physics resembles that of MEIS. The simulated spectra, assuming the full description as determined from the MEIS is also illustrated in Fig. 5 (b and c). In this case, the dielectric functions of Si and SiO_2 were used as input. From these functions the inelastic mean free path was calculated along with the energy loss that the projectile suffers

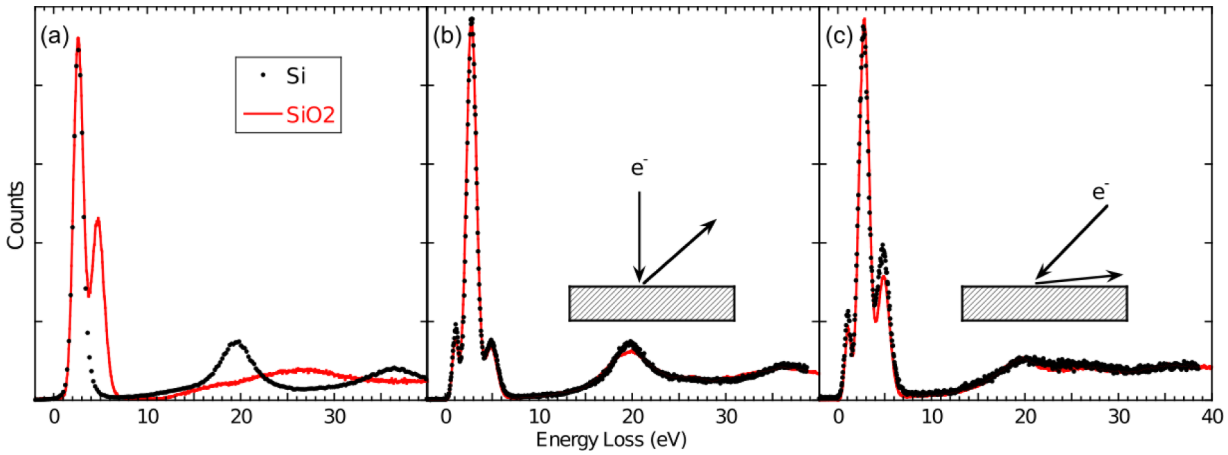

Fig. 5. Scattering of 40 keV electrons at an angle of 135°. Spectra obtained for thick, bulk Si (dots) and SiO_2 (line) samples (a). S1 spectra measured with the electron beam impinging along the surface normal (b), *i.e.* in a bulk-sensitive geometry, and with the sample rotated over 34° (c), *i.e.* in a surface-sensitive geometry. The measured spectra (dots) are compared with simulations (lines) using the full description model of S1 presented in Table 1. Qualitatively the spectrum is well described, both for the elastic peak and the energy loss part of the spectrum.

Table 1
Full description of S1 and S2 best fitting models. Stoichiometry, thickness, density and As dose of the models shown in Fig. 3 (a and e) are reported for each layer.

Layer	Stoichiometry	Thickness (nm)	Density (g/cm^3)	As dose (atoms/cm^2)
S1 (wet clean)				
1st	SiO_2	11.0	2.00	—
2nd	$As_{0.01}Si_{0.33}O_{0.65}$	2.75	2.03	1.8×10^{14}
3rd	$As_{0.15}Si_{0.85}$	0.8	2.88	5.9×10^{14}
4th	$As_{0.06}Si_{0.94}$	4.5	2.55	1.3×10^{15}
S2 (wet clean and thermal treatment)				
1st	SiO_2	12.4	1.83	—
2nd	$As_{0.01}Si_{0.33}O_{0.65}$	1.2	1.86	7.9×10^{13}
3rd	$As_{0.14}Si_{0.86}$	1.5	2.85	1.0×10^{15}
4th	$As_{0.06}Si_{0.94}$	3.5	2.55	1.0×10^{15}
5th	$As_{0.04}Si_{0.96}$	1.0	2.47	2.0×10^{14}
6th	$As_{0.02}Si_{0.98}$	4.3	2.40	4.3×10^{14}

if an inelastic event occurs. Note that for perpendicular incidence the Si plasmon dominates the loss spectrum, whereas for the surface-sensitive geometry both Si and SiO_2 loss features contributes significantly, in both the experiment and the simulation. This is a direct evidence that the electronic structure of the top layer resembles that of SiO_2, and the electronic structure of the substrate represented that of Si.

4. Summary and conclusion

We have measured the atomic composition of the PLAD implanted samples and explored the potential of the Coulomb explosion of H_2^+ molecule to determine absolute thicknesses and densities. Two sets of samples were studied, one had only underwent a wet clean process after the implantation (S1) and the other had undergone wet clean and thermal treatment processes (S2). We measured on average a density reduction of 13 % in the SiO_2 overlayer. Cross-checking by comparing results from MEIS based on the Coulomb explosion methodology and from electron techniques (TEM/EDS and ERBS) show good agreement. However, the Coulomb explosion method is unique for determining absolute thicknesses and densities opening new perspectives for the use of ion beam at intermediate energies in microelectronics.

Acknowledgment

This work was performed under the auspices of Brazilian Coordination for the Improvement of Higher Education Personnel (CAPES, 88887.176042/2018-00), Brazilian National Council for Scientific and Technological Development (CNPq, 117750/2017-4 and 165047/2015-1), and Brazilian National Institute of Surface Engineering (INES). We would like to thank staff members at Varian Semiconductor Equipment Business Unit, Applied Materials in the Plasma Doping Group for preparing the samples.

References

[1] T. Song, W. Rim, J. Jung, G. Yang, J. Park, S. Park, Y. Kim, K. Baek, S. Baek, S. Oh, S.-K. Oh, J. Jung, S. Kim, G. Kim, J. Kim, Y. Lee, S.-P.S.J.S. Yoon, K.-M. Choi, H. Won, J. Park, A 14 nm FinFET 128 Mb SRAM with V_{MIN} enhancement techniques for low-power applications, IEEE J. Solid-State Circ. 50 (1) (2015) 158–169.
[2] N. Loubet, T. Hook, P. Montanini, C.K. Yeung, S.K. Kanakasabapathy, M. Guillom, T. Yamashita, J.-G. Zhang, X.Y. Miao, J.H. Wang, A.B. Young, R. Chao, M. Kang, Z. Liu, S. Fan, B.M. Hamieh, S. Sieg, Y. Mignot, W. Xu, S. Seo, J. Yoo, S. Mochizuki, M. Sankarapandian, O.N. Kwon, A.S. Carr, A.S. Greene, Y.-W. Park, J. Frougier, R. Galatage, R. Bao, J. Shearer, R. Conti, H.H. Song, D. Lee, X. Kong, Y. Xu, A. Arceo, Z. Bi, P. Xu, R. Muthinti, J. Li, R.C. Wong, D.F. Brown, P. Oldiges, R. Robison, J.A. Arnold, N.T. Felix, S. Skordas, J.G. Gaudiello, T. Standaert, H. Jagannathan, D. Corliss, M.-H. Na, A. Knorr, T. Wu, D. Gupta, S. Lian, R. Divakaruni, T. Gow, C. Labelle, S.-B. Lee, V. Paruchuri, H. Bu, M. Khare, Stacked nanosheet gate-all-around transistor to enable scaling beyond FinFET, 2017 Symposium on VLSI Technology, IEEE, 2017, pp. T230–T231.
[3] S. Reboh, R. Coquand, S. Barraud, N. Loubet, N. Bernier, G. Audoit, J. Rouviere, E. Augendre, J. Li, J. Gaudiello, N. Gambacorti, T. Yamashita, O. Faynot, Strain, stress, and mechanical relaxation in fin-patterned Si/SiGe multilayers for sub-7 nm nanosheet gate-all-around device technology, Appl. Phys. Lett. 112 (5) (2018) 051901.
[4] P.A.W. van der Heide, Critical need and future directions of SIMS depth profiling in CMOS fabrication, J. Vac. Sci. Technol. B 36 (3) (2018) 03F105.
[5] W. Vandervorst, J.L. Everaert, E. Rosseel, M. Jurczak, T. Hoffman, P. Eyben, J. Mody, G. Zschätzsch, S. Koelling, M. Gilbert, T. Poon, J. del Agua Borniquel, M. Foad, R. Duffy, B.J. Pawlak, Conformal doping of FinFETs: a fabrication and metrology challenge, AIP Conf. Proc. 1066 AIP, 2008, pp. 449–456.
[6] D. Gupta, Plasma immersion ion implantation (PIII) process–physics and technology, Int. J. Adv. Technol. 2 (4) (2011) 471–490.
[7] A. Anders, From plasma immersion ion implantation to deposition: a historical perspective on principles and trends, Surf. Coat. Technol. 156 (1) (2002) 3–12.
[8] D.M. Goebel, R.J. Adler, D.F. Beals, W.A. Reass, Handbook of Plasma Immersion Ion Implantation and Deposition, Andre Anders, New York, 2000.
[9] W. Vandervorst, C. Fleischmann, J. Bogdanowicz, A. Franquet, U. Celano, K. Paredis, A. Budrevich, Dopant, composition and carrier profiling for 3D structures, Mater. Sci. Semiconduct. Process. 62 (2017) 31–48.
[10] J.P. Barnes, A. Grenier, I. Mouton, S. Barraud, G. Audoit, J. Bogdanowicz, C. Fleischmann, D. Melkonyan, W. Vandervorst, S. Duguay, N. Rolland, F.Vurpillot, D.Blavette, Atom probe tomography for advanced nanoelectronic devices: current status and perspectives, Scr. Mater. 148 (2018) 91–97.
[11] S.M. Shubeita, R.C. Fadanelli, J.F. Dias, P.L. Grande, Determination of film thicknesses through the breakup of H_2^+ ions, Surf. Sci. 608 (2013) 292–296.
[12] J. England, J. van den Berg, A. Rossall, Use of TRIDYN and medium energy ion scattering to calibrate an industrial arsenic plasma doping process, J. Vac. Sci. Technol. B 37 (3) (2019) 031206.
[13] J. van den Berg, A. Rossall, J. England, Characterization of arsenic plasma doping and postimplant processing of silicon using medium energy ion scattering, J. Vac.

Sci. Technol. B 37 (3) (2019) 032901.
[14] T. Miller, L. Godet, G.D. Papasouliotis, V. Singh, Plasma doping—Enabling technology for high dose logic and memory applications, AIP Conference Proceedings, 1066 AIP, 2008, pp. 457–460.
[15] R.G. Smeenk, R.M. Tromp, H.H. Kersten, A.J.H. Boerboom, F.W. Saris, Angle resolved detection of charged particles with a novel type toroidal electrostatic analyser, Nucl. Instr. Meth. B 195 (3) (1982) 581–586.
[16] R.M. Tromp, H.H. Kersten, E. Granneman, F.W. Saris, R. Koudijs, W.J. Kilsdonk, A new UHV system for channeling/blocking analysis of solid surfaces and interfaces, Nucl. Instr. Meth. B 4 (1) (1984) 155–166.
[17] K.J. Mighell, Parameter estimation in astronomy with Poisson-distributed data. I. The χ^2_γ statistic, Astrophys. J. 518 (1) (1999) 380.
[18] M.A. Sortica, P.L. Grande, G. Machado, L. Miotti, Characterization of nanoparticles through medium-energy ion scattering, J. Appl. Phys. 106 (11) (2009).
[19] G.G. Marmitt, PowerMEIS simulation code, 2019, http://tars.if.ufrgs.br/.
[20] L.F.S. Rosa, P.L. Grande, J.F. Dias, R.C. Fadanelli, M. Vos, Neutralization and wake effects on the Coulomb explosion of swift H_2^+ ions traversing thin films, Phys. Rev. A 91 (4) (2015) 042704.
[21] M.R. Went, M. Vos, Rutherford backscattering using electrons as projectiles: underlying principles and possible applications, Nucl. Instr. Meth. B 266 (2008) 998–1011.
[22] D.S. Gemmell, J. Remillieux, J.C. Poizat, M.J. Gaillard, R.E. Holland, Z. Vager, Evidence for an alignment effect in the motion of swift ion clusters through solids, Phys. Rev. Lett. 34 (23) (1975) 1420.
[23] W. Brandt, A. Ratkowski, R.H. Ritchie, Energy loss of swift proton clusters in solids, Phys. Rev. Lett. 33 (22) (1974) 1325.
[24] J.F. Ziegler, J.P. Biersack, The stopping and range of ions in matter, Treatise on Heavy-Ion Science, Springer, 1985, pp. 93–129.
[25] J.F. Ziegler, The stopping and range of ions in matter, 2013, http://www.srim.org/.
[26] W.K. Chu, J.W. Mayer, M.A. Nicolet, Backscattering Spectrometry, Academic Press, 1987.
[27] J.B. Marion, F.C. Young, Nuclear Reaction Analysis, Graphs and Tables, North Holland Publishing Co, Amsterdam, 1968.
[28] R.P. Pezzi, C. Krug, P.L. Grande, E.B.O. da Rosa, G. Schiwietz, J.R. Israel, Analytical energy loss distribution for accurate high resolution depth profiling using medium energy ion scattering, Appl. Phys. Lett. 92 (16) (2008) 164102.
[29] S.M. Shubeita, M.A. Sortica, P.L. Grande, J.F. Dias, N.R. Arista, Signature of plasmon excitations in the stopping ratio of fast hydrogen clusters, Phys. Rev. B 77 (11) (2008) 115327.
[30] N.E. Koval, A.G. Borisov, L.F.S. Rosa, E.M. Stori, J.F. Dias, P.L. Grande, D. Sánchez-Portal, R.D. Muiño, Vicinage effect in the energy loss of H_2 dimers: experiment and calculations based on time-dependent density-functional theory, Phys. Rev. A 95 (6) (2017) 062707.
[31] S. Heredia-Avalos, R. Garcia-Molina, J.M. Fernández-Varea, I. Abril, Calculated energy loss of swift He, Li, B, and N ions in SiO_2, Al_2O_3, and ZrO_2, Phys. Rev. A 72 (5) (2005) 052902.
[32] J. England, W. Möller, J. van den Berg, A. Rossall, W. Min, J. Kim, Combining dynamic modelling codes with medium energy ion scattering measurements to characterise plasma doping, Nucl. Instr. Meth. B 409 (2017) 60–64.
[33] S. Qin, M.P. Bradley, P.L. Kellerman, Faraday dosimetry characteristics of PIII doping processes, IEEE Trans. Plasma Sci. 31 (3) (2003) 369–376.
[34] W. Möller, W. Eckstein, TRIDYN – A TRIM simulation code including dynamic composition changes, Nucl. Instr. Meth. B 2 (1984) 814–818.